

Multiscale modeling of droplet deposition and solidification dendrite growth during DED-Arc additive manufacturing of a nickel-based superalloy

Qingyu Zhang(张庆宇), Zhixian Chen(陈志贤), Rong Wang(王荣), Pengcheng Huan(环鹏程), Dongke Sun(孙东科), and Xiaonan Wang(王晓南)

Citation: Chin. Phys. B, 2026, 35 (**8**): 084701. DOI: 10.1088/1674-1056/ae2671
http://cpb.iphy.ac.cn; http://iopscience.iop.org/cpb

What follows is a list of articles you may be interested in

Generation of droplet group based on an external electromagnetic valve in a microfluidic chip

Dong Wang(王东), Xiaonan Li(李啸楠), Jiayi Zhou(周佳怡), Liyu Liu(刘雳宇), and Guo Chen(陈果)
Chin. Phys. B, 2025, 34 (**12**): 124702. DOI: 10.1088/1674-1056/ade063

Morphological analysis for thermodynamics of cavitation collapse near fractal solid wall

Minglei Shan(单鸣雷), Yu Yang(杨雨), Xuefen Kan(阚雪芬), Cheng Yin(殷澄), and Qingbang Han(韩庆邦)
Chin. Phys. B, 2024, 33 (**6**): 064701. DOI: 10.1088/1674-1056/ad3343

Discussion on interface deformation and liquid breakup mechanism in vapor-liquid two-phase flow

Xiang An(安祥), Bo Dong(董波), Ya-Jin Zhang(张雅瑾), and Xun Zhou(周训)
Chin. Phys. B, 2023, 32 (**9**): 094702. DOI: 10.1088/1674-1056/acc78e

Dynamic evolution of low-viscosity fuel particle distribution driven by constant flow

Zhong-Kun Yang(杨仲坤), Gao-Jun An(安高军), Xi-Meng Xu(徐曦萌), Zhe Zheng(郑哲), Yong-Xu Wang(王永旭), Li-Feng Xie(解立峰), Dan Zhang(张丹), and Bin Li(李斌)
Chin. Phys. B, 2023, 32 (**7**): 074701. DOI: 10.1088/1674-1056/acc8c2

Oxidation during the production of FGH4095 superalloy powders by electrode induction-melt inert gas atomization

Shan Feng(峰山), Min Xia(夏敏), Chang-Chun Ge(葛昌纯)
Chin. Phys. B, 2018, 27 (**4**): 044701. DOI: 10.1088/1674-1056/27/4/044701

Multiscale modeling of droplet deposition and solidification dendrite growth during DED-Arc additive manufacturing of a nickel-based superalloy

Qingyu Zhang(张庆宇)[1], Zhixian Chen(陈志贤)[1], Rong Wang(王荣)[1], Pengcheng Huan(环鹏程)[2], Dongke Sun(孙东科)[3], and Xiaonan Wang(王晓南)[1,†]

[1] *School of Metallic Materials and Advanced Manufacturing, Soochow University, Suzhou* 215137, *China*
[2] *School of Automotive Engineering, Suzhou University of Technology, Suzhou* 215500, *China*
[3] *School of Mechanical Engineering, Southeast University, Nanjing* 211189, *China*

(Received 9 September 2025; revised manuscript received 20 November 2025; accepted manuscript online 2 December 2025)

The evolutions of droplet morphology on the macroscale and solidification microstructure on the microscale, during direct energy deposition (DED)-Arc additive manufacturing of a nickel-based alloy, are simulated by developing a multiscale model based on the lattice Boltzmann and cellular automaton models. The macroscopic model is quantitatively validated by modeling the time-dependent phase interface position and temperature distribution for a classical Stefan problem of phase change in the multiphase system. In the simulation of droplet deposition, it is found that the contact line length between the deposited droplet and substrate is proportional to a defined overall factor, $d_{\mathrm{D}}^2 \cdot |\boldsymbol{u}|^2 \cdot \Delta T \cdot (1+\cos\theta_0)$, composed of droplet size (d_{D}), impact velocity ($\boldsymbol{u}$), temperature difference (ΔT), and intrinsic contact angle (θ), respectively. The overall factor allows one to evaluate the contact line length prior to the experiment, which is significant for heat transfer efficiency and formability of the additive manufacturing products. The evolution of temperature distribution during multilayer droplet deposition is obtained, and the calculated cooling rate ($\sim$ 800 K/s) and temperature gradient ($\sim$ 1 K/m) accord well with the typical data in the literature. By mapping the macroscopic temperature field data into the microscopic model through multidimensional linear interpolation, the growth of dendrites during solidification of the pillar-shaped product is reproduced. Both the simulation and experimental results show that the solidification dendrites present coarse columnar patterns, with several millimeters in length extending multiple deposition layers. This work not only elucidates the complex interactions among droplet impact dynamics, convective heat transfer, solidification/melting, and wetting phenomena in droplet deposition, but also provides an alternative for the predictions of the DED-Arc additive manufacturing formability, as well as the evolution of convections, temperature, and solidification microstructure.

Keywords: droplet deposition, DED-Arc additive manufacturing, solidification microstructure, numerical modeling, nickel-based superalloy

PACS: 47.55.Ca, 47.55.D–, 91.60.Ed, 07.05.Tp

DOI: 10.1088/1674-1056/ae2671 **CSTR:** 32038.14.CPB.ae2671

1. Introduction

Nickel-based superalloys can preserve high mechanical strength, desirable creep and fatigue resistances, and good corrosion endurance in elevated temperature environments (*e.g.*, $>$ 650 °C), which are widely applied in fields of aerospace industry, power generation equipment like gas turbines, and refinery chemical equipment.[1] Owing to the inherent merits of additive manufacturing, such as high flexibility in geometric design of products and excellent capability in integration of different materials, the studies of additive manufacturing have attracted considerable interest in both academia and industry.[2] In recent years, the application of additive manufacturing on the fabrication of nickel-based superalloy products has also received lots of attention in the research community of materials processing.[3,4] Among various additive manufacturing techniques, the direct energy deposition (DED)-Arc additive manufacturing uses arc energy and wires as the heat source and raw materials, respectively, which has high deposition rate and is favorable for the rapid fabrication of large-sized products.[5] Through the process of droplet transfer in DED-Arc additive manufacturing, a high-temperature droplet is generated and detaches from the wire. Then, it impacts and melts the substrate, or the top of formerly deposited material, until completely solidified in the following cooling process. It is noted that this droplet deposition process occurs in a solid/liquid/gas (S/L/G) multiphase system, including complex interactions among droplet dynamics, heat transfer, phase change (melting/solidification), and wetting phenomena. Thus, the full understanding of droplet deposition in the DED-Arc additive manufacturing requires appropriate analyses of the above-mentioned factors and their interactions. It is known that the process of droplet deposition in DED-Arc additive manufacturing takes place within a very

†Corresponding author. E-mail: wxn@suda.edu.cn

© 2026 Chinese Physical Society and IOP Publishing Ltd. All rights, including for text and data mining, AI training, and similar technologies, are reserved.

short period. Aided by modern devices of experimental observation, *e.g.*, high-speed camera and thermal infrared imager, one can obtain the transient data of droplet morphology, fluctuations, and temperature distribution on liquid/gas (L/G) interfaces.[6,7] However, it is still challenging to measure the significant data of temperature field, flow field, and concentration field within the droplet. On the other hand, the direct observation of the evolving solid/liquid (S/L) interfaces in dendritic solidification by using the synchrotron-based x-ray tomography is somewhat difficult in DED-Arc additive manufacturing, because it requires complex devices of encapsulation.[8,9]

With the tremendous progress in computing power, multiscale modeling based on physical mechanisms, as well as data-driven methods, has been developed to understand and predict the information of temperature field, concentration evolution, convection distribution, and solidification microstructure formation in molten pools produced by various types of additive manufacturing.[10–15] Liu *et al.*[10] developed a macroscopic model for investigating the phenomena of heat accumulation in metal droplet-based additive manufacturing. The evolution of convective temperature field, solid fraction, and droplet morphology of an aluminum alloy was visualized in the simulations. Yet, the intrinsic contact angle of the droplet on solidified parts of the product was set as constant as 90°. This configuration is different from physical realities, since the deposited droplet and solidified parts of the product belong to the same material and the wettability should be perfect. Liang *et al.*[11] built a macroscopic model composed of the calculations of computational fluid dynamics (CFD) and stress evolution during a wire feeding-based laser additive manufacturing. The convection and temperature distributions in the molten pool, as well as temperature and stress distributions on the solidified part, were reproduced and analyzed in detail. Wang *et al.*[12] studied the evolution of temperature distribution and TiC particles in the molten pool of DED-Arc additive manufacturing of an aluminum alloy, by using CFD coupled with the Lagrange particle model incorporated in the software of Ansys Fluent. However, the microscopic modeling of solidification microstructure evolution was not included in the articles of Liang *et al.*[11] and Wang *et al.*[12] A multiscale model was proposed by Wang *et al.*[13] to investigate heat transfer, dendrite growth, and solute segregation during DED-Arc additive manufacturing of an IN718 nickel-based alloy. The macroscopic convective heat transfer model was implemented by using the software of Ansys Fluent, in which the L/G interface was tracked by the volume of fluid (VOF) algorithm. On the microscale, a phase field was applied to simulate the microstructure evolution. In their work, the data of cooling rate and temperature gradient were read from the results of macroscopic modeling, and were then input into the microscopic phase field model as constants. As a result, the evolution of temperature field revealed in the macroscopic modeling was not incorporated in the microscopic simulations. It is noted that even though most of the macroscopic models could include the various mechanisms during the process of droplet deposition, *e.g.*, droplet impact dynamics, convective heat transfer, phase change, and wetting phenomena, the interactive effects of these factors on the determination of droplet morphologies still require future investigation.

Unlike the front-tracking multiphase CFD models, *e.g.*, the VOF algorithm, the multiphase lattice Boltzmann (LB) method separates the different fluid phases by adding local interactions among the surrounding fluid particles, so that there is no need to take efforts in tracking the position of the evolving interfaces.[16] Owing to this specific nature, the multiphase LB modeling has been widely used in the studies such as freezing dynamics of droplets,[17] wetting phenomena,[18] and medical treatments.[19] Regarding the simulations of microstructure evolution during solidification, on the other hand, the cellular automaton (CA) method has the advantages of high computational efficiency and simplicity in coding, which is one of the most popular methods for the descriptions of solidification dendrite growth in various materials processing techniques.[20,21] In our previous articles, several models have been developed by coupling the CA and LB methods for the simulations of dendritic solidification assisted by ultrasound,[22] porosity formation and dendrite growth of an aluminum alloy,[23] convective dendrite growth of a nickel-based superalloy,[24] and solute mixing during dissimilar-filler welding.[25]

In the present work, based on the multiphase LB model and the CA method, a multiscale model is developed for the simulations of deposited droplet morphology on the macroscale, and solidification microstructure patterns on the microscale, during the DED-Arc additive manufacturing of an IN718 nickel-based superalloy. The competitive interactions among droplet impact dynamics, convective heat transfer, solidification/melting, and wetting phenomena were reproduced, and their contributions to the droplet morphology are analyzed in detail. The growth of the columnar dendrites during the multilayer droplet deposition process is revealed by the microscopic modeling and compared with the experimental results. As compared to the related research reported in the literature, the specificity of our work is, on the one hand, to explicitly correlate the synthesis effects of the above-listed complex interactions on the solidification behavior of the deposited droplets by proposing an overall factor. On the other hand, the multiscale scheme in this work rigorously bridges the microscopic solidification microstructure model and the macroscopic temperature field model by using the multidimensional interpolation algorithm. Thus, the evolving temperature his-

tory of each local area during droplet deposition could be input into the microscopic model, instead of artificially arranging the values of cooling rate and temperature gradient. The simulation results could not only elucidate the fundamental physics underlying the multiphase system during the process of droplet deposition, but also provide guidance for the control of the formability and microstructure of the DED-Arc additive manufacturing products.

2. Model description and governing equations

2.1. Model description

In the present study, the process of DED-Arc additive manufacturing of an IN718 alloy is simulated by using a two-dimensional multiscale model. In the macroscale part, the multiphase LB model is adopted to reproduce the evolution of flow and temperature fields during droplet deposition.[26,27] To reproduce the effects of rapid solidification during the DED-Arc process, especially for the first droplet impacting the base metal, the kinetics of solidification is calculated by using the Scheil–Gulliver model.[28] In the microscale part, on the other hand, the CA model, coupled with the finite-difference-method (FDM), is used to describe the process of dendrite growth and solute diffusion.[29] The data of temperature history are produced by the macroscale model, which has included the influence of flow field during droplet impacting and pile-up for producing the multilayer product. The temperature data are imported into the CA model through the algorithms of linear interpolation in multidimensions, *i.e.*, x, y directions in the spatial dimension and one freedom in the time dimension. In the microscopic CA model, the (Kurz–Giovanola–Trivedi) KGT model is used to govern the S/L migration driven by the undercooling.[29] The codes of the multiscale model are written by using the C++ computer language.

3. Multiphase lattice Boltzmann method for the macroscopic modeling

For simulating the L/G flow phenomena interacting with the solid phase on the macroscale, the pseudopotential multiphase LB model with the multi-relaxation-time (MRT) scheme is used.[26,27] The LB model assumes that the L/G fluids are composed of particles, and the various flow behaviors can be reproduced by a statistical treatment of the particle distribution functions. In the D2Q9 (two dimensions, nine velocities) system, the time evolution of distribution functions of fluid particles is written as

$$\begin{aligned} & f_i(\boldsymbol{x}+\boldsymbol{e}_i\Delta t, t+\Delta t) \\ = \; & f_i(\boldsymbol{x},t) - \left(\boldsymbol{M}^{-1}\boldsymbol{\Lambda}\boldsymbol{M}\right)_{ij}\left(f_j - f_j^{\mathrm{eq}}\right) + F_i'\Delta t, \\ & i,j = 0,1,\ldots,8, \end{aligned} \tag{1}$$

where f_i and f_i^{eq} are the distribution function and the corresponding equilibrium distribution function, respectively. $\boldsymbol{x}$, t, and Δt are the position, time, and time step, respectively. The forms of transformation matrices, $\boldsymbol{M}$ and $\boldsymbol{M}^{-1}$, can be found elsewhere.[30] F_i' represents the forcing term. The diagonal matrix, $\boldsymbol{\Lambda}$, is composed of relaxation times

$$\boldsymbol{\Lambda} = \mathrm{diag}\left(\tau_\rho^{-1}, \tau_e^{-1}, \tau_\zeta^{-1}, \tau_j^{-1}, \tau_q^{-1}, \tau_j^{-1}, \tau_q^{-1}, \tau_\nu^{-1}, \tau_\nu^{-1}\right), \tag{2}$$

where τ_ν and τ_e are related to the dynamic and bulk viscosities, which are set to be $\tau_\nu = 4/5$ and τ_e =5/4, respectively. The other relaxation times are $\tau_\rho = \tau_j = 1$, $\tau_\zeta = 5/4$, and $\tau q = \tau_q = 10/11$, respectively. In Eq. (1), the discrete velocities, $\boldsymbol{e}_i$, are

$$\begin{aligned} & [\boldsymbol{e}_0, \boldsymbol{e}_1, \boldsymbol{e}_2, \boldsymbol{e}_3, \boldsymbol{e}_4, \boldsymbol{e}_5, \boldsymbol{e}_6, \boldsymbol{e}_7, \boldsymbol{e}_8] \\ = & \begin{bmatrix} 0 & c & 0 & -c & 0 & c & -c & -c & c \\ 0 & 0 & c & 0 & -c & c & c & -c & -c \end{bmatrix}, \end{aligned} \tag{3}$$

where $c = \Delta x/\Delta t$ is the lattice speed, and Δx is the lattice size. In this work, the values of Δx and Δt are $\Delta x = 1$ lu (lattice unit) and $\Delta t = 1$ ts (time step), respectively, where lu and ts are the units in the LB model.

Through linear transformations of $\boldsymbol{m} = \boldsymbol{M}\cdot\boldsymbol{f}$ and $\boldsymbol{m}^{\mathrm{eq}} = \boldsymbol{M}\cdot\boldsymbol{f}^{\mathrm{eq}}$, the distribution functions and the corresponding equilibrium ones are transformed from the velocity space to the moment space. $\boldsymbol{m}^{\mathrm{eq}}$ are written as

$$\begin{aligned} m^{\mathrm{eq}} = \; & \rho[1, -2+3|u|^2, 1-3|u|^2, u_x, \\ & -u_x, u_y, -u_y, u_x^2 - u_y^2, u_x u_y]^{\mathrm{T}}, \end{aligned} \tag{4}$$

where ρ and $\boldsymbol{u}$ are density and velocity, calculated by $\rho = \sum_i f_i$ and $\rho\boldsymbol{u} = \sum_i \boldsymbol{e}_i f_i + \boldsymbol{F}\Delta t/2$, respectively.

By left multiplying $\boldsymbol{M}$ on the right-hand side of Eq. (1), it is rewritten as

$$\boldsymbol{m}^* = \boldsymbol{m} - \boldsymbol{\Lambda}(\boldsymbol{m} - \boldsymbol{m}^{\mathrm{eq}}) + \Delta t\left(\boldsymbol{I} - \frac{\boldsymbol{\Lambda}}{2}\right)\boldsymbol{S}, \tag{5}$$

where $\boldsymbol{I}$ and $\boldsymbol{S}$ are the unit tensor and forcing term, respectively. The streaming of the particle distribution functions is described as $\boldsymbol{f}(\boldsymbol{x}+\boldsymbol{e}_i\Delta t, t+\Delta t) = \boldsymbol{f}^*(\boldsymbol{x},t)$ with the transformation of $\boldsymbol{f}^* = \boldsymbol{M}^{-1}\boldsymbol{m}^*$. The form of $\boldsymbol{S}$ is

$$\begin{aligned} \boldsymbol{S} = \; & [0, 6u\cdot F + 12\varepsilon|F|^2/\left(\psi^2\Delta t(\tau_e - 0.5)\right), \\ & -6u\cdot F - 12\varepsilon|F|^2/\left(\psi^2\Delta t(\tau_\zeta - 0.5)\right), \\ & F_x, -F_x, F_y, -F_y, 2\left(u_x F_x - u_y F_y\right), u_x F_y + u_y F_x]^{\mathrm{T}}, \end{aligned} \tag{6}$$

where $\varepsilon = 0.09$ is applied in this work and it is consistent with the literature.[25] $\boldsymbol{F}$ represents the force acting on the fluid particles, which includes the intermolecular interaction force $\boldsymbol{F}_m$, the gravitational force $\boldsymbol{F}_g$, and Marangoni force caused by surface tension gradient at the L/G interface $\boldsymbol{F}_{\mathrm{Marangoni}}$. $\boldsymbol{F}_m$ is calculated by

$$\boldsymbol{F}_m(\boldsymbol{x},t) = -G\psi(\boldsymbol{x},t)\sum_i \omega_i \psi(\boldsymbol{x}+\boldsymbol{e}_i\Delta t, t)\boldsymbol{e}_i, \tag{7}$$

where ω_i are the weight coefficients, *i.e.*, $\omega_{1,2,3,4} = 1/3$ and $\omega_{5,6,7,8} = 1/12$. ψ is the pseudopotential function and computed by $\psi = \sqrt{2(P_{\rm EOS} - \rho c_{\rm s}^2)/G}$, where $c_{\rm s}^2 = 1/3$ is the square of the lattice sound speed. G is the interaction strength, which is taken as $G = -1$. $P_{\rm EOS}$ is the equation of state, given by

$$P_{\rm EOS} = \frac{\rho R T'}{1-b\rho} - \frac{a\rho^2\left[1+(1-\sqrt{T'/T_{\rm c}})(0.37464+1.5226\omega'-0.26992)\omega'^2\right]^2}{1+2b\rho-b^2\rho^2}, \tag{8}$$

where T' controls the strength of the fluid-fluid interaction and the liquid-gas density ratio. According to the work of Yuan and Schaefer,[31] the parameter $T_{\rm c}$ is equal to 0.072922, and the coefficients of a, b, R, and w' are selected to be $a = 2/49$, $b = 2/21$, $R = 1$, and $w' = 0.344$, respectively. In the present study, $T' = 0.86T_{\rm c}$ is adopted, and the liquid-gas density ratio is around 20.

At the L/G interface, the non-uniform temperature distributions produce surface tension gradients, leading to Marangoni convection and thus influencing the heat and mass transport in the molten pool. The Marangoni force is calculated by[32]

$$\boldsymbol{F}_{\rm Marangoni} = \sigma_{\rm T} A \frac{\partial T}{\partial \boldsymbol{s}} = \sigma_{\rm T} A \left(\nabla T \cdot \boldsymbol{s}\right) \boldsymbol{s}, \tag{9}$$

where $\sigma_{\rm T}$ is the temperature coefficient of surface tension. A and $\boldsymbol{s}$ denote the area and tangential unit vector of the L/G interface, respectively. It should be noted that the L/G interface must be tracked for the calculation of Eq. (9), since the determination of $\boldsymbol{s}$ requires the evolving position of the L/G interface. In this work, the local data of $\boldsymbol{s}$ are obtained by 90° counterclockwise rotating the corresponding normal vector of the L/G interface, which is written

$$\boldsymbol{s} = \begin{pmatrix} \cos 90^\circ & -\sin 90^\circ \\ \sin 90^\circ & \cos 90^\circ \end{pmatrix} \cdot \boldsymbol{n}, \tag{10}$$

where $\boldsymbol{n}$ is the normal vector and is computed according to the gradient of density, $\boldsymbol{n} = \nabla\rho/|\nabla\rho|$.

An improved virtual-density scheme is applied in the present work to regulate the intrinsic contact angle, θ_0, of a droplet on a solid substrate.[26] This scheme could avoid the drawback of producing unphysical thick mass-transfer layers near the solid boundaries, which is a common issue in previous studies. The formula for the virtual density is

$$\rho_{\rm w}(\boldsymbol{x}) = \begin{cases} \varphi\rho_{\rm ave}(\boldsymbol{x}), & \varphi \geq 1 \quad \text{for} \quad \theta_0 \leq 90^\circ, \\ \rho_{\rm ave}(\boldsymbol{x}) - \Delta\rho, & \Delta\rho \geq 0 \quad \text{for} \quad \theta_0 > 90^\circ, \end{cases} \tag{11}$$

where φ and $\Delta\rho$ are constants. A limiter is applied to bound the value of $\rho_{\rm w}(\boldsymbol{x})$, given by $\rho_{\rm g} \leq \rho_{\rm w}(\boldsymbol{x}) \leq \rho_{\rm l}$, where $\rho_{\rm g}$ and $\rho_{\rm l}$ are the equilibrium densities of the gas and liquid phases, respectively. When $\varphi = 1$ or $\Delta\rho = 0$, the above formula reduces to $\rho_{\rm w}(\boldsymbol{x}) = \rho_{\rm ave}(\boldsymbol{x})$, in which $\rho_{\rm ave}(\boldsymbol{x})$ is calculated by

$$\rho_{\rm ave}(\boldsymbol{x}) = \frac{\sum_i \omega_i \rho(\boldsymbol{x}+\boldsymbol{e}_i\Delta t, t) s(\boldsymbol{x}+\boldsymbol{e}_i\Delta t, t)}{\sum_i \omega_i s(\boldsymbol{x}+\boldsymbol{e}_i\Delta t, t)}, \tag{12}$$

where $s(\boldsymbol{x}+\boldsymbol{e}_i\Delta t)$ is an indicator function that is equal to 1 or 0 for a fluid or a solid node, respectively. Table 1 lists the values of φ and $\Delta\rho$ used in this work for the simulation of droplets with various θ_0 impacting the solid base surface.

Table 1. Values of φ and $\Delta\rho$ used for obtaining various θ_0 in the present work.

φ	$\Delta\rho$	θ_0
1.65	0	0°
1.49	0	30°
1.22	0	60°
1.00	0	90°
1.00	0.47	120°
1.00	0.86	150°

Another set of distribution functions is introduced in the present work to calculate the temperature field. According to the lattice Bhatnagar–Gross–Krook (LBGK) approximation, the evolution of the temperature distribution function, $h_i(\boldsymbol{x},t)$, can be written as[27]

$$\begin{aligned} & h_i(\boldsymbol{x}+\boldsymbol{e}_i\Delta t, t+\Delta t) - h_i(\boldsymbol{x},t) \\ = & -\frac{1}{\tau_{{\rm T},k}}\left[h_i(\boldsymbol{x},t) - h_i^{\rm eq}(\boldsymbol{x},t)\right] + H_i(\boldsymbol{x},t) + C_i(\boldsymbol{x},t) \\ & i = 0,\ 1,\ldots,8, \end{aligned} \tag{13}$$

where $h_i^{\rm eq}(\boldsymbol{x},t)$ represents the equilibrium distribution function for temperature field computation. $H_i(\boldsymbol{x},t)$ is the temperature source term induced by latent heat during solidification and melting. $C_i(\boldsymbol{x},t)$ is a correction term calculated by $C_i = 3\left(1 - \frac{1}{2\tau_{{\rm T},k}}\right)\omega_{{\rm T},i}\partial_t(T\boldsymbol{u})$, where $\omega_{{\rm T},i}$ are the weight coefficients for the calculation of temperature field, given by $\omega_{{\rm T},0} = 4/9$, $\omega_{{\rm T},1-4} = 1/9$, and $\omega_{{\rm T},5-8} = 1/36$, respectively. The local temperature can be obtained by $T = \sum_{i=0}^{8} h_i$. The heat diffusion coefficient, α_k, is determined by the relaxation time, $\tau_{{\rm T},k}$, and is given by

$$\alpha_k = \frac{1}{3}\left(\tau_{{\rm T},k} - \frac{1}{2}\right)\Delta t, \tag{14}$$

where the subscript 'k' denotes 's', 'l', or 'g', representing solid, liquid, and gas phases, respectively. In the present work, the heat diffusivities of the gas and liquid phases are assumed to be $\alpha_{\rm g} = 0.01\alpha_{\rm l}$.

In Eq. (13), $h_i^{\rm eq}(\boldsymbol{x},t)$ is calculated by[27]

$$h_i^{\rm eq}(x,t) = \omega_{{\rm T},i}T(x,t)\left[1 + 3\frac{\boldsymbol{e}_i \cdot \boldsymbol{u}(x,t)}{c^2}\right]. \tag{15}$$

The flow velocity vector necessarily includes the contributions of convection to the temperature field evolution. Note that $\boldsymbol{u}$ is derived from the flow field calculation by the multiphase LB model, which provides connections between the MRT multiphase LB model and the solute transport computation by using the LBGK model.

In the simulation of solidification in the macroscopic modeling, the Scheil-Gulliver equation is applied to relate local solid fraction (f_s) and temperature (T), which is given by[28]

$$f_\mathrm{s} = 1 - \left(\frac{T_\mathrm{m} - T}{T_\mathrm{m} - T_\mathrm{l}}\right)^{1/(k_\mathrm{p}-1)}, \tag{16}$$

where T_m is the melting point of pure nickel. T_l and k_p are the liquidus temperature and solute partitioning coefficient of an IN718 alloy, respectively. According to the evolution of f_s in each node, the melting and solidification phenomena are reproduced. The temperature source term in Eq. (13) can be computed as

$$H_i(\boldsymbol{x},t) = \frac{\omega_{\mathrm{T},i}\Delta f_\mathrm{s}\Delta H}{C_\mathrm{p}}, \tag{17}$$

where Δf_s is the increment of solid fraction in each node. ΔH and C_p are the latent heat and specific heat, respectively. At the S/L interface, C_p is calculated by $C_\mathrm{p} = f_\mathrm{s}C_{\mathrm{p,s}} + (1-f_\mathrm{s})C_{\mathrm{p,l}}$, where $C_{\mathrm{p,s}}$ and $C_{\mathrm{p,l}}$ are the specific heats of the solid and liquid phases, respectively.

In the flow field and temperature field calculations, the periodic and zero-flux boundary conditions are used on the domain walls, and a bounce-back boundary condition is adopted on the S/L boundaries.

3.1. Cellular automaton model for microscopic modeling

The phenomena of melting and solidification during DED-Arc additive manufacturing are simulated by a CA model on the microscopic scale. At the S/L interface, the solid fraction increment is evaluated by

$$\Delta f_\mathrm{s} = v \cdot \frac{\Delta t}{\Delta x} \cdot g, \tag{18}$$

where v is the migration velocity of the S/L interface. g is the geometrical factor for decreasing the grid anisotropy, given by

$$\begin{aligned} g &= \min\left(\left(\sum_{m=1}^{4} S_m^{\mathrm{I}} + \frac{1}{\sqrt{2}}\sum_{m=1}^{4} S_m^{\mathrm{II}}\right)\Big/3\ ,\ 1\right), \\ S^{\mathrm{I}}, S^{\mathrm{II}} &= \begin{cases} 0 & (f_\mathrm{s} < 1), \\ 1 & (f_\mathrm{s} = 1), \end{cases} \end{aligned} \tag{19}$$

where S^{I} and S^{II} are the states of the nearest and next-nearest neighboring cells.

According to the KGT model, v in Eq. (18) is determined by the local undercooling, δT, at the S/L interface, which is

$$v = a(\delta T)^b, \tag{20}$$

where a and b are the kinetic parameters. For an IN718 alloy, the values of a and b are 1.2754×10^{-7} and 3.0, respectively. These values are selected according to the work of Hunziker *et al.*[33] $b = 3.0$ in the present work is a little bit different from $b = 3.05$ calculated by Hunziker *et al.*[33] This is because the melting phenomenon simulation requires the definitional domain of $\delta T < 0$, which can be fulfilled by $b = 3.0$. Otherwise, the CA model can only cover the solidification kinetics with $\delta T > 0$. δT is calculated by

$$\delta T = (T_\mathrm{m} + m_\mathrm{l}\cdot C_\mathrm{l}^*) - \Gamma K_\mathrm{w} - T^*, \tag{21}$$

where K_w is the weighted curvature of the S/L interface, and Γ is the Gibbs–Thomson coefficient. m_l is the slope of the liquidus line. C_l^* is the local actual liquid composition at the S/L interface. Additionally, the effects of v on m_l and k_p are considered.[24] The actual temperature on each CA grid, T^*, is calculated by the linear interpolation algorithm. The output parameters for solving Eqs. (18)–(21) in the microscopic CA model are the evolving local data on each grid, including local solid fraction increment, S/L interface migration velocity, local undercoolings, *etc*. As a result, the local data of solid fraction, $f_\mathrm{s}(x,y)$, can be obtained and it evolves with time and position, which present the morphological evolution of the solidification dendrites.

Figure 1 illustrates the schematic map for the interpolation algorithm on spatial and temporal dimensions. Suppose $T(x_\mathrm{p}, y_\mathrm{p}, t)$ is the target temperature on a CA grid at any time, which is required in the microscopic modeling. At the time of t_1, the temperature data of $T(x_1, y_1, t_1)$, $T(x_2, y_1, t_1)$, $T(x_1, y_2, t_1)$, and $T(x_2, y_2, t_1)$ are obtained from the macroscopic modeling. Through the bilinear interpolation, the temperature of $T(x_\mathrm{p}, y_\mathrm{p}, t_1)$ can be derived by

$$\begin{aligned} T\left(x_\mathrm{p},y_\mathrm{p},t_1\right) &= \frac{y_2-y_\mathrm{p}}{y_2-y_1}\left[\frac{x_2-x_\mathrm{p}}{x_2-x_1}T\left(x_1,y_1,t_1\right)\right. \\ &\quad \left.+\frac{x_\mathrm{p}-x_1}{x_2-x_1}T\left(x_2,y_1,t_1\right)\right] \\ &\quad +\frac{y_\mathrm{p}-y_1}{y_2-y_1}\left[\frac{x_2-x_\mathrm{p}}{x_2-x_1}T\left(x_1,y_2,t_1\right)\right. \\ &\quad \left.+\frac{x_\mathrm{p}-x_1}{x_2-x_1}T\left(x_2,y_2,t_1\right)\right], \end{aligned} \tag{22}$$

where the values of x and y are the corresponding coordinates. At the time of t_2, similarly, the temperature of $T(x_\mathrm{p}, y_\mathrm{p}, t_2)$ can also be obtained. Then, the target temperature of $T(x_\mathrm{p}, y_\mathrm{p}, t)$ is computed through the linear temporal interpolation, which is written as

$$\begin{aligned} T\left(x_\mathrm{p},y_\mathrm{p},t\right) &= T\left(x_\mathrm{p},y_\mathrm{p},t_1\right) \\ &\quad +\frac{T\left(x_\mathrm{p},y_\mathrm{p},t_2\right)-T\left(x_\mathrm{p},y_\mathrm{p},t_1\right)}{t_2-t_1}(t-t_1). \end{aligned} \tag{23}$$

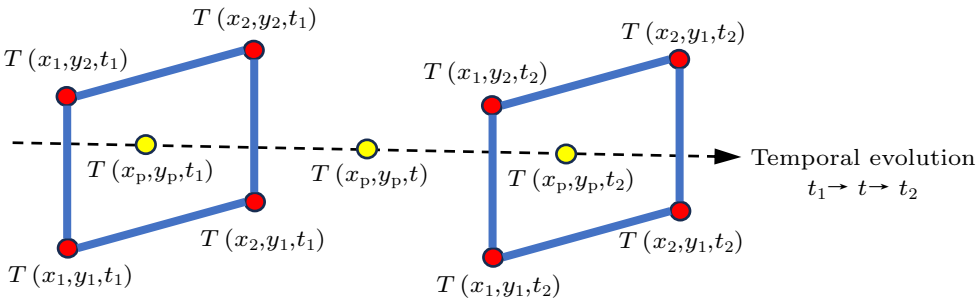


Fig. 1. Schematic sketch for the illustration of the multidimensional linear interpolation algorithm.

As described in our previous work,[34] the solute transport is calculated by solving the equation of Fick's second law. Zero-flux boundary conditions are implemented on all walls of the computational domains.

In the present work, the materials of the deposited droplet and the substrate are arranged as the same. Thus, the thermophysical properties of the droplet and the substrate are identical. The physical parameters used in the present work for microscopic and macroscopic modeling of an IN718 nickel-based alloy are listed in Table 2.

Table 2. Physical parameters of an IN718 alloy used in the present work.[24,29,32]

Symbol	Definition and units	Value
Γ	Gibbs–Thomson coefficient (K·m)	3.65×10^{-7}
D_l	diffusion coefficient in liquid (m^2/s)	3×10^{-9}
D_s	diffusion coefficient in solid (m^2/s)	1×10^{-12}
α_s	heat diffusion coefficient of solid (m^2/s)	7.35×10^{-6}
α_l	heat diffusion coefficient of liquid (m^2/s)	6.17×10^{-6}
α_g	heat diffusion coefficient of gas (m^2/s)	6.17×10^{-8}
m_l	equilibrium liquidus slope (K/wt.%)	-10.5
T_m	melting point of the pure Ni (K)	1726
k_p	equilibrium partition coefficient of Nb	0.48
μ	viscosity of liquid (Pa·s)	6.2×10^{3}
$C_{p,s}$	heat capacity of solid (J/kg/K)	720
$C_{p,l}$	heat capacity of liquid (J/kg/K)	512
ΔH	latent heat (J/kg)	2.1×10^{5}
ρ_s	density of solid (kg/m^3)	8.19×10^{3}
ρ_l	density of liquid (kg/m^3)	7.62×10^{3}
σ_T	Marangoni coefficient (N/m/K)	-1.1×10^{-4}

4. Results

4.1. Model validation

In the multiscale model, the microscopic model has been validated by the previous work of the present authors.[22] Nevertheless, the validity of the macroscopic model, implemented by the multiphase LB model, needs to be demonstrated. Before performing the simulation of melting and solidification phenomena during the DED-Arc process, the classical Stefan problem of phase change is simulated using the macroscopic LB model, and the simulation results of the interface position and temperature distributions varying with time are compared with the analytical predictions. The schematic sketch of the Stefan problem is shown in Fig. 2. Suppose a semi-infinite slab $x \geq 0$ initially filled with liquid at the temperature of $T > T_m$, where T_m is the melting/solidification point of the pure substance. At the position of $x = 0$, the temperature remains constant at T_b, which is lower than T_m. Therefore, directional solidification occurs from the position of $x = 0$ to $x > 0$. The time evolution of the S/L interface position, $X(t)$, and the temperature distribution, $T(t, x)$, can be quantitatively predicted by the analytical model proposed in the work of Solomon.[35]

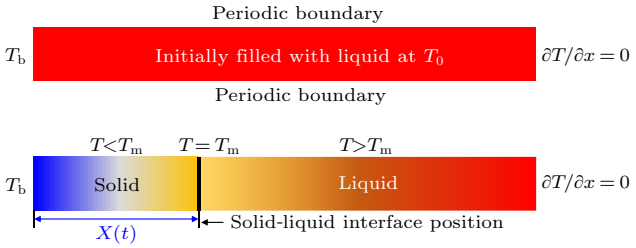


Fig. 2. Schematic sketch of the Stefan problem for solidification of a pure substance.

The solutions of the analytical model for predicting the S/L interface position, $X(t)$, and the temperature distribution, $T(x, t)$, are as follows:[35]

$$X(t) = 2\lambda(\alpha_s t)^{1/2}, \tag{24}$$

$$T(x,t) = \begin{cases} \dfrac{T_m}{\mathrm{Erf}(\lambda)}\mathrm{Erf}\left[x/(4\alpha_s t)^{1/2}\right], & 0 \leq x \leq X(t): \text{solid}, \\ T_0 - \dfrac{(T_0 - T_m)\,\mathrm{Erfc}\left[x/(4\alpha_l t)^{1/2}\right]}{\mathrm{Erfc}\left[\lambda(\alpha_s/\alpha_l)^{1/2}\right]}, & x > X(t): \text{liquid}, \end{cases} \tag{25}$$

where α_s is the heat diffusion coefficient of the solid phase. The value of λ in Eqs. (24) and (25) can be obtained by solving the following equation:

$$-\frac{\kappa_l \alpha_s^{1/2}(T_0 - T_m)\exp\left(-\lambda^2 \alpha_s/\alpha_l\right)}{\kappa_s \alpha_l^{1/2} T_m \mathrm{Erfc}\left[\lambda\left(\alpha_s/\alpha_l\right)^{1/2}\right]} = -\frac{\exp\left(-\lambda^2\right)}{\mathrm{Erfc}\left(\lambda\right)} + \frac{\lambda \Delta H \pi^{1/2}}{C_{p,s} T_m}, \tag{26}$$

where κ_s and κ_l are the thermal conductivities of the solid and liquid phases, respectively. In this part, the dimensionless physical parameters in the macroscopic LB model and analytical model are determined according to the work of Solomon,[35] which are $T_m = 170$, $T = 340$, $T_b = 0$, $\Delta H = 30$, $\rho_s = \rho_l = 1$, $\kappa_s = \kappa_l = 1$, and $C_{p,s} = C_{p,l} = 10$, respectively. In the LB simulation, the domain size is set to be 20000×2 lu with 1 lu = 0.1 mm.

Figure 3 displays the evolution of S/L interface position and temperature distributions, obtained from the macroscopic LB model (symbols) and the analytical model (lines). As shown in Fig. 3(a), the value of X increases with time, denoting the ongoing solidification phenomenon from the left wall to the right-hand side. The temperature curves also present rising trends, as displayed in Fig. 3(b), and gradually decrease as the solidification proceeds.

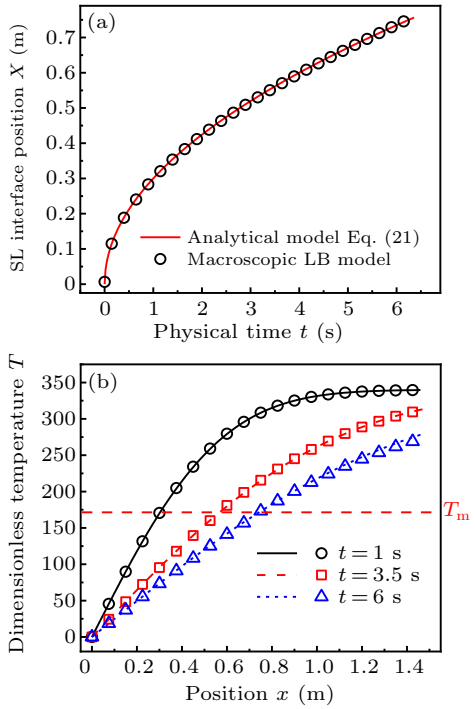


Fig. 3. Comparisons of (a) evolution of the S/L interface position and (b) temperature distribution at different times, obtained from the macroscopic LB simulation and analytical model.

4.2. Macroscopic modeling of droplet impact, solidification, melting, and heat transfer

The behavior of droplet impingement during the DED-Arc process is coherently governed by complex interactions among droplet spreading dynamics, heat transfer, melting/solidification, and wetting phenomena. In order to elucidate the effects of the above-mentioned mechanisms individually, the simulation of droplet impingement is firstly performed by the macroscopic LB model eliminating the melting/solidification mechanism. The initial temperatures of the solid base, atmosphere, and droplet are set to be 423 K, 298 K, and 2273 K, respectively. The grid size is 1 lu = 10 μm, and the diameter of the droplet is $d_D = 120$ lu (1.2 mm). The impacting velocity of the droplet is set to be 0.08 lu/ts. Figure 4 exhibits the morphologies of droplets that have different intrinsic contact angles on the base, θ_0, shown by the S/L/G phases and temperature fields, respectively. These snapshots are at the same time (4600 ts) in the simulations of droplet impingement. The various intrinsic contact angles are obtained by setting different values of φ and $\Delta\rho$ as listed in Table 1. When the intrinsic contact angle is low, the droplet tends to expand on the solid base, so that the droplet has a large contact area. As the intrinsic contact angle increases, however, the droplet is likely to shrink and to depart from the solid base. As shown in Fig. 4(b), for the case of $\theta_0 = 30°$, the temperature of the droplet is obviously lower than that of the other cases. In Fig. 4, the effects of melting and solidification of the deposited droplets are not incorporated. In the practical DED-Arc process, however, the coupled phenomena of droplet deformation, heat transfer, and variation of final droplet morphology during solidification should be more complex.

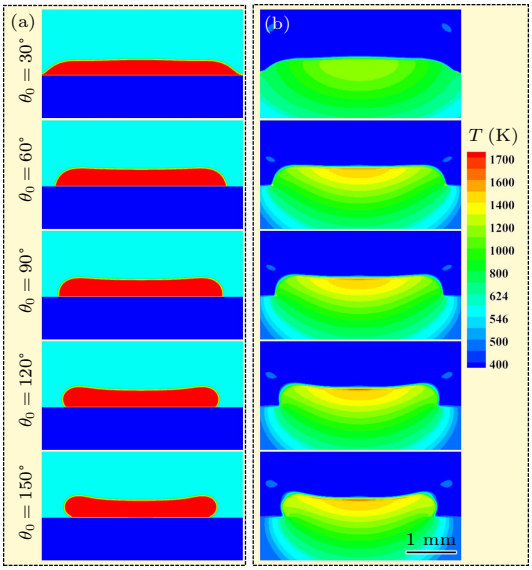


Fig. 4. Snapshots of (a) droplet morphologies and (b) temperature distributions for droplets having various intrinsic contact angles (θ_0) after impacting the base metal, simulated by the macroscopic LB model without the melting and solidification mechanisms. The snapshots are all taken at the simulation time of 4600 ts.

The following simulations are then carried out by using the macroscopic model considering the melting and solidification mechanisms, governed by Eqs. (16) and (17). Figure 5 visualizes the simulated evolution of the single droplet impingement and solidification shown by different phases and temperature field, respectively. In this case, the intrinsic contact angle between the liquid droplet and base metal is set to be $\theta_0 = 0°$, mimicking that the base metal and the deposited droplets belong to the same material (IN718 alloy). The value of θ_0 could be regulated when using different base metal materials in the simulations.[10] The downward impinging velocity

of the droplet is 0.1 lu/ts. The initial temperatures of the base metal and droplet are 423 K and 2073 K, respectively, so that the temperature difference is 1650 K in the beginning of the simulation. As shown in Figs. 5(a) and 5(f), the hot droplet is falling with the vertically downward velocity. The droplet then impacts the base surface, so that some local velocities at the droplet bottom generally turn into the horizontal direction, which can be seen in Figs. 5(b) and 5(c). Meanwhile, it is found in Figs. 5(g) and 5(h) that heat transfer occurs once the droplet contacts the solid surface. As a result, the temperature of the solid phase near the contacting area gradually becomes higher, see Figs. 5(g)–5(j), whereas the bottom part of the droplet is cooled by the base surface. The solidification phenomenon takes place as the local temperature of the droplet becomes lower than the liquidus temperature. Even though the solidification completes in a short time, the L/G interface is still fluctuating, and these mechanisms coherently control the final morphology of the solidified droplet. As observed in Figs. 5(d) and 4(e), the former L/G interface solidifies earlier than the upper interior of the droplet. This is attributed to the fact that the large temperature gradient at the L/G interface also leads to local heat transfer from the droplet to atmosphere. Then, the droplet is enveloped by solid and it leaves a liquid pocket that solidifies at last during the entire deposition process.

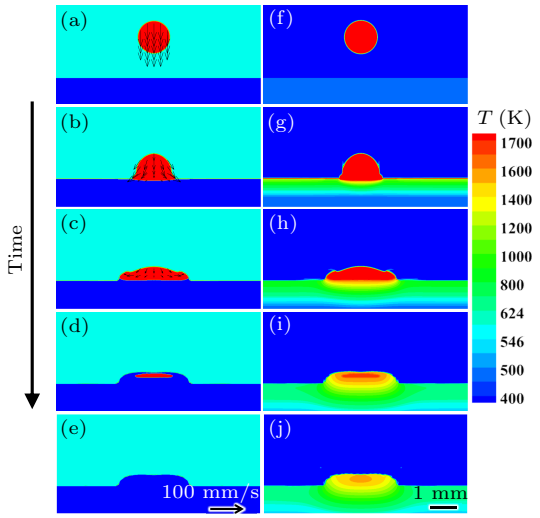


Fig. 5. Evolution of (a)–(e) droplet morphology and (f)–(j) temperature field during single droplet impacting the base metal and the gradual solidification process. The intrinsic contact angle is 0°, and the arrows indicate the local velocities inside the droplet.

Figure 6 illustrates the morphologies of solidifying droplets that impinge on the solid base, as well as the corresponding temperature fields, simulated by the macroscopic LB model incorporating the melting and solidification mechanisms. Note that the intrinsic contact angles (θ) between the droplets and the solid base are set to be different. The corresponding apparent contact angles, θ, are also measured and labeled in Fig. 6. The other simulation conditions of the cases with $\theta = 30°$, 60°, 90°, 120°, and 150° keep the same as those of Fig. 6. It is worth noting that the obtained apparent angles are higher than the intrinsic contact angles. On the other hand, the lengths of the contact lines (l) between the droplets and substrate differ when θ is regulated. It is apparent that the contact line length becomes smaller as θ increases.

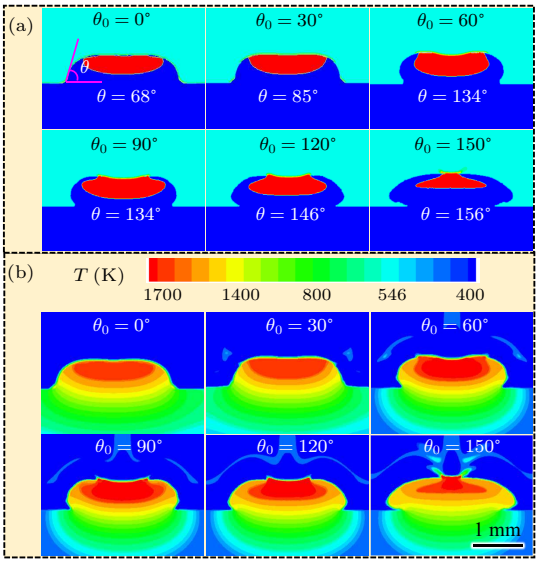


Fig. 6. Snapshots of (a) droplet morphologies and (b) temperature distributions for droplets having various intrinsic contact angles after impacting the base metal, simulated by the macroscopic LB model with the melting/solidification mechanisms. The snapshots are all taken at the LB simulation time of 3000 ts.

In order to elucidate the determination of the contact line length by various factors, *i.e.*, droplet diameter (d_D), droplet impinging velocity ($\boldsymbol{u}$), initial temperature difference (ΔT), and intrinsic contact angle (θ) between droplet and substrate, 21 sets of simulations are implemented using the macroscopic LB model by regulating the above-described values. An overall factor is proposed to describe the contributions of the various physical quantities, which is written as $d_D^2 \cdot |\boldsymbol{u}|^2 \cdot \Delta T \cdot (1 + \cos\theta_0)$. Figure 7 displays the value of the contact line length varying with the overall factor. Note that the scatters are the results obtained from the macroscopic LB model, while the line represents the corresponding linear fit. It is revealed that the contact line length almost increases with the overall factor in a linear manner.

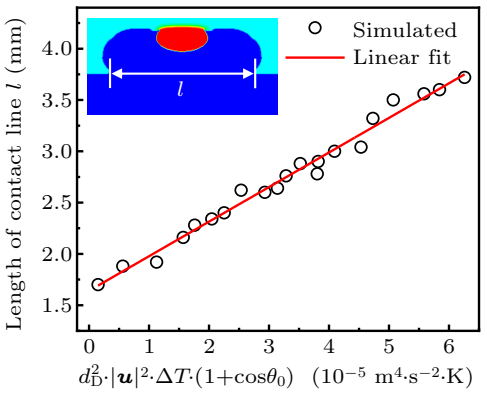


Fig. 7. Length of contact line between deposited droplet and substrate varying with an overall factor composed by droplet diameter (d_D), droplet impinging velocity ($\boldsymbol{u}$), initial temperature difference between droplet and substrate (ΔT), and intrinsic contact angle (θ_0).

Figure 8 displays the LB simulation results of the multilayer droplet deposition shown by the temperature field. The domain consists of 400×700 lu with 1 lu = 20 μm. In order to eliminate the effect of heat accumulation and to improve the forming quality, the interval time between each droplet is different. The droplets are set at the LB simulation times of 4100 ts, 10900 ts, 17900 ts, 25400 ts, and 36500 ts, which correspond to the physical times of 0.20 s, 0.54 s, 0.88 s, 1.25 s, and 1.80 s, respectively. The intrinsic contact angle, initial velocities of the droplets, and the initial temperatures are identical with those of Fig. 5. As shown in Fig. 8(a), the droplet melts the solid phase produced by the former droplet that solidifies. The droplet continues to expand and shrink due to the impingement behavior until it completely solidifies, see Fig. 8(b). It can be seen in Figs. 8(c) and 8(d) that a pillar is fabricated as the droplet pileup and solidification proceed. As displayed by the temperature field evolution in Fig. 8, apparent temperature gradients are seen between the liquid droplet and solid regions, which determines the direction of heat transfer. As a result, the temperature of the substrate increases obviously as compared to the initial state. The macroscopic simulation results of temperature field in Fig. 8 could reasonably reproduce the interactions between heat transfer and melting/solidification phenomena during the multilayer droplet deposition process in the S/L/G coexisting system.

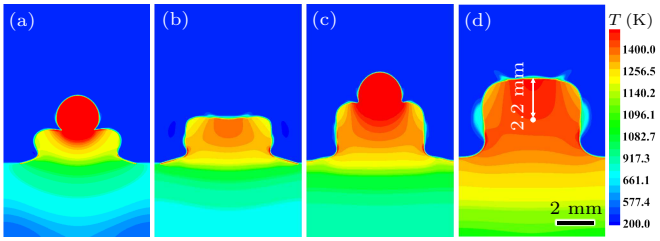


Fig. 8. Simulated evolution of multilayer droplet deposition shown by temperature field at the LB simulation times of (a) 11700 ts, (b) 17800 ts, (c) 26300 ts, and (d) 54400 ts, corresponding the physical times of 0.58 s, 0.88 s, 1.29 s, and 2.68 s, respectively.

The time evolutions of temperature, T, and temperature gradient, T_G, at a local position during the DED-Arc additive manufacturing are extracted from the simulation results, as exhibited in Fig. 9, to analyze the solidification conditions. The selected local position is denoted by the white spot in Fig. 8(d), which is located in the middle on the horizontal direction and 2.2 mm below the pillar top. In Fig. 9(a), it is seen that the increase of temperature is due to the impact and deposition of the hot droplets, while the temperature decrease is caused by heat transfer during solidification. In the temperature interval ranging from the solidus temperature (1615 K) and the liquidus temperature (1673 K) of the IN718 alloy, the cooling rate is evaluated from the slope of the T–t curve in Fig. 9(a), which is about 800 K/s. For the temperature gradient (T_G), as shown in Fig. 9(b), the peak values also appear when the hot droplets impinge and melt the solidified top of the pillar. However, the temperature gradient quickly resumes to be stable once the solidification initiates. During the solidification process of the local region, the value of the temperature gradient is less than 1 K/m.

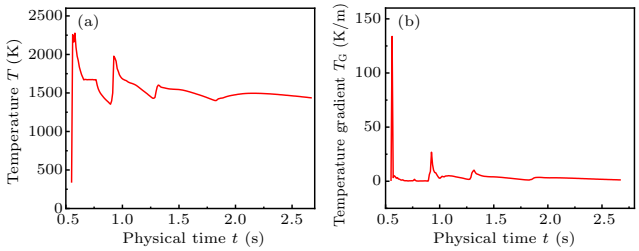


Fig. 9. Time evolutions of (a) temperature and (b) temperature gradient of the local position denoted by the white spot in Fig. 8(d).

4.3. Microscopic modeling of solidification microstructure

As described in Fig. 8, the macroscopic LB simulations provide the temperature history during droplet impingement, pileup, and solidification. The temporal and spatial temperature data are then interpolated into the microscopic CA model to visualize the growth of columnar dendrites and concentration distribution evolution of solute Nb of the IN718 alloy. In the microscopic CA simulation of solidification microstructure, the grid size is set to be 2 μm, and the computational domain consists of 1500×4000 CA grids. On the temporal dimension, 532 sets of evolving temperature distributions, spanning the physical time of 2.68 s, are imported in the CA model. In order to compare the simulation results with experiments, the DED-Arc additive manufacturing of an IN718 nickel-based alloy is carried out in this study. The details of the experimental equipment could be found elsewhere in our previous work.[36] A thin-wall component is fabricated by using the DED-Arc additive manufacturing. After polishing and etching the cross-section of the sample, an Olympus SZX10 optical microscopy is used to observe the morphology of the solidification microstructure. Figure 10 exhibits the simulated evolution of columnar dendrites in the case of multilayer droplet deposition, as well as the comparison with experimental metallograph. As shown by the evolving Nb concentration fields, displayed on the left-hand sides of Figs. 10(a) and 10(c), the fully liquid regions present nearly uniform Nb concentration distributions. Nearby the solidification front, however, the solute concentration fields show heterogeneous patterns due to the solute partitioning effects. After solidification, it can be seen that the Nb concentrations in the middle region are lower than the surrounding areas, presenting non-negligible segregation within the component. The panels on

the right-hand sides of Figs. 10(a)–10(d) exhibit the evolution of columnar dendrites during solidification/melting in the case of multilayer droplet deposition simulation. It is obvious that the columnar dendrites originate from the bottom of the pillar, and grow toward the high temperature direction along the temperature gradient. Even though some grains are eliminated in the process of dendritic growth, most of the columnar dendrites present coarse morphologies, with the length of several millimeters extending multiple deposition layers. Figure 10(e) is the experimental metallograph showing the coarse columnar dendrites of the thin-wall product fabricated by the DED-Arc additive manufacturing. It is shown that the columnar dendrites grow epitaxially toward the higher temperature direction, presenting identical morphologies with the simulation results.

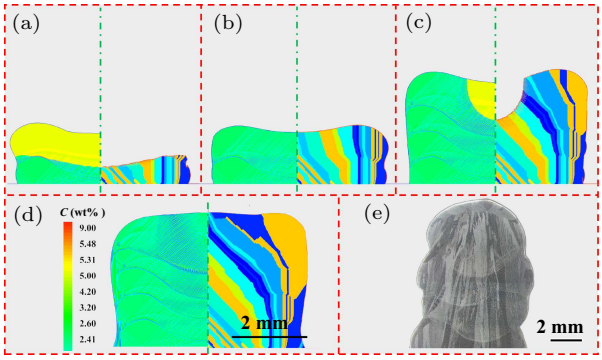


Fig. 10. Images of (a)–(d) simulated evolution of solidification microstructure by using the microscopic CA model and (e) coarse columnar dendrites in the experimental metallograph. The left- and right-hand sides of (a)–(d) are shown by the concentration field of solute Nb and grain orientations, respectively.

5. Discussion

Figure 3 displays the comparison of the simulation results of the S/L interface position and temperature distributions occurring in the classical Stefan problem of phase change, obtained from the proposed macroscopic model (symbols) and the analytical model (lines),[35] respectively. The excellent coincidence demonstrates the soundness of the LB model and the correctness of the codes in the present work, which gains reliability of the simulation results of the following cases.

It is understandable in Fig. 4(a) that the good intrinsic is beneficial for increasing the length of the contact line. Additionally, the variation of the wettability could also influence the heat release of the hot droplet in the cooling period. Namely, the temperature of the droplet with the best wettability is obviously lower than that of the other cases, see Fig. 4(b), in which all of the temperature distribution snapshots are taken at the same simulation time. This is because more heat flux could transfer to the solid base that has a lower temperature through the larger contact area within a certain period.

The simulation results in Fig. 5 reveal that the solidification of the deposited droplet not only takes place from bottom to top, but also occurs concurrently on the top of the droplet, *i.e.* the L/G interface. Consequently, the concurrent solidification leaves a transient liquid pocket in the upper area. This phenomenon was also observed in the literature regarding DED-Arc additive manufacturing.[37,38] In fact, the formation of the liquid pocket tends to occur at the top layer of the deposited droplets in multilayer droplet-based additive manufacturing cases. Owing to the effect of heat accumulation, the rate of heat transfer from the hot droplet to the lower layers becomes weaker, which decelerates the solidification from the bottom to the top. Once the heat transfer rate at the L/G interface is high enough to trigger the local solidification, the transient liquid pocket might be produced. Thus, the formation of the transient liquid pocket is determined by the competition of heat transfer at different local regions of the deposited droplet. It is considered that the existence of transient liquid pocket is favorable for improving forming accuracy, but might lead to negative effects including shrinkage and cracking defects.

In addition to the fact that the contact line length (l) and apparent contact angle (θ) are changed by setting different intrinsic wettability (see Fig. 6), the values of l and θ are coherently determined by the competitions among heat transfer, phase transformation (melting/solidification), multiphase flow dynamics (*e.g.*, droplet impinging velocity), and intrinsic contact angle. Once the local region of the contact area solidifies, the morphologies of the deposited droplets and the values of l and θ could be acquired. As compared to the apparent contact angle, the contact line length has more significant influences on heat transfer and S/L phase transformation in the case of multilayer depositions in DED-Arc additive manufacturing. This is because the contact line length determines the rate of heat dissipation from the deposited droplets to the cooler substrate.

In the proposed overall factor set as the x-axis of Fig. 7, $d_{\mathrm{D}}^2 \cdot |\boldsymbol{u}|^2 \cdot \Delta T \cdot (1+\cos\theta_0)$, the value of $d_{\mathrm{D}}^2 \cdot |\boldsymbol{u}|^2$ is directly proportional to the kinetic energy due to droplet impingement in the two-dimensional system. The initial temperature difference between droplet and substrate, ΔT, is related to the heat energy released during cooling and solidification. The term of $(1+\cos\theta)$ in the overall factor correlates the contact line length with the intrinsic wettability, which ranges from 0 to 1. Thus, the proposed overall factor integrates the physical meanings of kinetic energy, heat energy, and intrinsic wettability. As a result of competition among multiphase fluid dynamics, heat transfer, S/L phase transformation, and wetting behavior, the bounding feature between the solidified droplet and sub-

strate, *e.g.*, the contact line length, is finally determined. Thus, one can evaluate the contact line length by using the proposed overall factor prior to the experiment, which is significant for heat transfer efficiency and formability of additive manufacturing products.

The fluctuation of the T–t curve in Fig. 9(a) exhibits that the measured peak temperatures gradually decrease with time. As more upper droplets impact the pillar, the heating effect on the local position becomes weaker, so that the cooling rate of the local position is gradually decreased. Accordingly, the peak temperatures measured at the local position are lower when later droplets deposit, as compared to the ones generated by the earlier droplets. In addition, it is revealed in Fig. 9(a) that there is a short plateau of the temperature curve as the first droplet impacts and solidifies. This plateau is caused by the effect of solidification latent heat, which alleviates the continuous cooling trend of the temperature curve. The temperature continues to decrease once the first droplet fully solidifies, until the second droplet arrives. However, as more droplets impact, the temperature variation due to latent heat could not be detected at that position gradually. Thus, the plateau is nearly unidentified as the second and latter droplets solidify. It is noted that the values of cooling rate ($\sim$ 800 K/s) and temperature gradient ($\sim$ 1 K/m) obtained from Fig. 9 are on the same magnitudes of the corresponding data in DED-Arc additive manufacturing reported in the literature.[39] These levels of cooling rate and temperature gradient generate millimeter-sized coarse columnar dendrites in the additive manufacturing product, as illustrated by both the simulation and experimental results in Fig. 10. The formation of coarse columnar solidification microstructure will lead to severe anisotropy on aspect of mechanical property. The refinement of the solidification microstructure of IN718 products fabricated by DED-Arc additive manufacturing will be investigated through experiments and numerical modeling in our future work.

6. Conclusions

A multiscale model is proposed for reproducing the evolutions of flow field, temperature field, and columnar dendrite microstructure during droplet impingement and the melting/solidification phenomena in DED-Arc additive manufacturing of a nickel-based alloy. On the macroscale, the flow field is simulated by using the MRT multiphase LB model, while the temperature field is calculated by using the LBGK LB algorithm. The melting and solidification of the IN718 nickel-based alloy are described by using the Scheil–Gulliver model. On the microscale, the CA model is used to simulate microstructure evolution. The solute transfer in the microscopic modeling is calculated by solving the equation of Fick's second law. The coupling of the macroscopic and microscopic models is realized through the algorithms of linear interpolation in multidimensions.

The proposed macroscopic model is validated by comparing its simulation results with the analytical predictions regarding the S/L interface position and temperature, belonging to the classical Stefan problem of phase change. The excellent agreement between the simulated data obtained from the macroscopic model and the analytical model demonstrates the correctness of the proposed macroscopic model.

The macroscopic model is then applied to simulate the interactions among droplet impact dynamics, convective heat transfer, phase change (melting/solidification), and dynamic wetting phenomena during droplet impingement on the substrate. The morphological features of the solidified droplets are coherently determined by several factors including the droplet size (d_{D}), impact velocity ($\boldsymbol{u}$), droplet-substrate temperature difference (ΔT), and intrinsic contact angle (θ). The contact line length (l) between the deposited droplet and the substrate is found to be proportional to a defined overall factor, $d_{\mathrm{D}}^2 \cdot |\boldsymbol{u}|^2 \cdot \Delta T \cdot (1+\cos\theta_0)$. The relationship of $l \propto d_{\mathrm{D}}^2 \cdot |\boldsymbol{u}|^2 \cdot \Delta T \cdot (1+\cos\theta_0)$ could illustrate the contributions of kinetic energy, heat energy, melting/solidification, and intrinsic wettability to the bonding features of the deposited material and the substrate. In addition, the temperature histories and temperature gradient at a local position are extracted and analyzed in the case of multilayer droplet deposition. The cooling rate and temperature gradient are evaluated at levels of $\sim$ 800 K/s and $\sim$ 1 K/m, respectively, which compare well with the data reported in the literature. After interpolating the evolving data of the temperature field into the microscopic CA model, the growth of columnar dendrites is simulated during solidification in DED-Arc additive manufacturing. It is found that the large columnar dendrites occupy several layers of the product, agreeing well with the experimental metallograph. This study not only reveals the complex interactions among heat transfer, convection, melting/solidification, and wetting phenomena in the multiphase system during the DED-Arc additive manufacturing, but also provides a methodology for the predictions of formability and solidification microstructure of the IN718 nickel-based superalloy.

Acknowledgement

Project supported by the National Natural Science Foundation of China (Grant No. 52475389).

References

[1] Xia H X, Yang C and Xu Q Y 2021 *Spec. Cast. Nonferrous Alloys* **41** 1334

[2] Tan C L, Li R S, Su J L, Du D F, Du Y, Attard B, Chew Y X, Zhang H O, Lavernia E J, Fautrelle Y, Teng J and Dong A P 2023 *Int. J. Mach. Tools Manuf.* **189** 104032

[3] Xi N Y, Fang X W, Duan Y S, Zhang Q and Huang K 2022 *J. Manuf. Process.* **75** 1134

[4] Hosseini E and Popovich V A 2019 *Addit. Manuf.* **30** 100877

[5] Zhou J X, Dang L X, Zhang H Q, Yu T T, Mao S C, Duan W, Ji X Y, Shen X, Yin Y J and Li W 2025 *Dev. Appl. Mater.* **40** 1

[6] Huan P C, Wei X, Wang X N, Di H S, Chen Y, Zhang Q Y, Chen X M and Shen X J 2022 *Mater. Sci. Eng. A* **854** 143845

[7] Liu X Y, Di Y L, Wang G, Yuan Q Y and Rong Y M 2025 *Addit. Manuf.* **98** 104649

[8] Brown D W, Losko A, Carpenter J S, Clausen B, Cooley J C, Livescu V, Kenesei P, Park J S, Stockman T J and Strantza M 2020 *Metall. Mater. Trans. A* **51** 1379

[9] Lu W Q, Zhang N F, Ding Z Y, Hu Q D and Li J G 2022 *Trans. Nonferrous Met. Soc. China* **32** 2451

[10] Liu M L, Yi H, Cao H J, Huang R F and Jia L 2021 *Addit. Manuf.* **48** 102413

[11] Liang L J, Hu R Z, Wang J S, Huang A G and Pang S Y 2021 *J. Manuf. Process.* **69** 602

[12] Wang Y Q, Zhou X M, Xiong X C, Yuan Y L, Bai X W, Fu J J and Wu H H 2025 *Int. Commun. Heat Mass Transfer* **161** 108454

[13] Wang L, Ding J L, Zhang X T, Zhang K J, Li H, Ou W M, Peng Y and Wang K H 2025 *Int. J. Heat Mass Transfer* **238** 126455

[14] Cao Y H, Chen C Y, Guo K, Hu T, Xu S Z, Wang J and Ren Z M 2024 *Spec. Cast. Nonferrous Alloys* **44** 1454

[15] Willy H J, Li X W, Tan Y H, Chen Z, Cagirici M, Borayek R, Herng T S, Ong C Y A, Li C J and Ding J 2020 *Chin. Phys. B* **29** 048101

[16] Shi L, Xu S Z, Hou Y Q, Hu T, Wu Y Q, Chen C Y, Wang J and Ren Z M 2025 *Metall. Mater. Trans. B* **56** 5773

[17] Huang J X, Li H Q, Che J Q, Chai Z H, Wang L and Shi B C 2025 *Int. J. Heat Mass Transfer* **242** 126852

[18] Tang S, Li Q, Li W and Chen S 2024 *Langmuir* **40** 18142

[19] Lv Q Y, Lan L L, He B and Wen B H 2025 *Phys. Fluids* **37** 083364

[20] Zhang Y, Zhang S J, Li Y B and Li R 2025 *Acta Phys. Sin.* **74** 108102 (in Chinese)

[21] Tang S F, Wei J J, Yue Y X, Li P Y, Yao M and Wang X D 2025 *Acta Metall. Sin.* **61** 941

[22] Wang Z T, Zhang Q Y, Tan L K and Wang X N 2025 *Materials and Solidification* **1** 9580002

[23] Chen Y, Chen X M, Zhang Q Y, Zhu M F, Liu F, Wang X N, Nagaumi H and Yao Z J 2022 *JOM* **74** 2428

[24] Chen B Y, Zhang Q Y, Sun D K and Wang Z J 2022 *J. Cryst. Growth* **585** 126583

[25] Zhang Q Y, Dong Q P, Wang X N, Wang Z J, Sun D K, Zhu M F, Qian Y H and Nagaumi H 2020 *J. Mater. Res. Technol.* **9** 12080

[26] Li Q, Yu Y and Luo K H 2019 *Phys. Rev. E* **100** 053313

[27] Li Q, Zhou P and Yan H J 2017 *Phys. Rev. E* **96** 063303

[28] Kurz W and Fisher D J 1992 *Fundamentals of solidification*, 3rd edn. (Switzerland) p. 285

[29] Wang Z T, Chen Z X, Zhang Q Y and Wang X N 2025 *J. Cryst. Growth* **652** 128052

[30] Zhang Q Y, Sun D K, Zhang S H, Wang H and Zhu M F 2020 *Chin. Phys. B* **29** 078104

[31] Yuan P and Schaefer L 2006 *Phys. Fluids* **18** 042101

[32] Zhao Y F, Koizumi Y, Aoyagi K, Wei D X, Yamanaka K and Chiba A 2019 *Addit. Manuf.* **26** 202

[33] Hunziker O, Dye D and Reed R 2000 *Acta Mater.* **48** 4191

[34] Zhang Q Y, Fang H, Xue H, Pan S Y, Rettenmayr M and Zhu M F 2017 *Sci. Rep.* **7** 17809

[35] Solomon A 1966 *Math. Comput.* **20** 347

[36] Huan P C, Wang X N, Zhang Q Y, Di H S, Chen X M, Chen Y and Wei X 2022 *J. Mater. Res. Technol.* **17** 1831

[37] Zhang C X, Qiu Z J, Zhu H L, Wang Z Y, Muránsky O, Ionescu M, Pan Z X, Xi J T and Li H J 2021 *Metals* **12** 46

[38] Jang J, Van D and Lee S H 2022 *Addit. Manuf.* **55** 102831

[39] Liu Z Y, Zhao D D, Wang P, Yan M, Yang C, Chen Z W, Lu J and Lu Z P 2022 *J. Mater. Sci. Technol.* **100** 224